Chaos and Relaxation Oscillations in Spin-Torque Windmill Spiking Oscillators

R. Matsumoto,[1,*] S. Lequeux,[2,3] H. Imamura,[1] and J. Grollier[2]

[1] *National Institute of Advanced Industrial Science and Technology (AIST), Spintronics Research Center, Tsukuba, Ibaraki 305-8568, Japan*

[2] *Unité Mixte de Physique, CNRS, Thales, Univ. Paris-Sud, Université Paris-Saclay, Palaiseau 91767, France*

[3] *Univ. Grenoble Alpes, CEA, CNRS, Grenoble INP, INAC-SPINTEC, 38000 Grenoble, France*

(Received 3 October 2018; revised manuscript received 27 February 2019; published 30 April 2019)

Spintronic neurons that emit sharp voltage spikes are required for the realization of hardware neural networks enabling fast data processing with low power consumption. In many neuroscience and computer science models, neurons are abstracted as nonlinear oscillators. Magnetic nano-oscillators called spin-torque nano-oscillators are interesting candidates for imitating neurons at the nanoscale. These oscillators, however, emit sinusoidal waveforms without spiking while biological neurons are relaxation oscillators that emit sharp voltage spikes. Here, we propose a simple way to imitate neuron spiking in high-magnetoresistance nanoscale spin valves, where both magnetic layers are free and thin enough to be switched by spin torque. Our numerical-simulation results show that the windmill motion induced by spin torque in the proposed spintronic relaxation oscillator gives rise to spikes whose shape and frequency, set by the charging and discharging times, can be tuned through the amplitude of injected dc current. We also find that these devices can exhibit chaotic oscillations. Chaoticlike neuron dynamics has been observed in the brain, and it is desirable in some neuromorphic computing applications, whereas it should be avoided in others. We demonstrate that the degree of chaos can be tuned in a wide range by engineering the magnetic stack and anisotropies and by changing the dc current. The proposed spintronic relaxation oscillator is a promising building block for hardware neuromorphic chips, leveraging nonlinear dynamics for computing.

DOI: 10.1103/PhysRevApplied.11.044093

I. INTRODUCTION

Neuromorphic chips need several millions of neurons to run state-of-the-art neural networks [1]. Keeping these chips small therefore requires developing nanoscale artificial neurons. In many neuroscience and computer science models, neurons are abstracted as nonlinear oscillators [2–5]. Memristive oscillators (also called neuristors) [6], Josephson junctions [7], nanoelectromechanical systems [8], and magnetic nano-oscillators called spin-torque nano-oscillators [9–11] are interesting candidates for imitating neurons at the nanoscale. In particular, it has been shown experimentally that spin-torque nano-oscillators can implement hardware neural networks and perform cognitive tasks with high accuracy due to their large signal-to-noise ratio, their high nonlinearity, and enhanced ability to synchronize [12,13].

However, the microwave voltage signals delivered by these spin valves driven by spin torque are typically sinusoidal. In contrast, biological neurons are relaxation oscillators, based on two time scales: a long charging period followed by a short discharge period [14,15]. Their output consists of sharp voltage spikes of fixed amplitude with a frequency that depends on the amplitude of the inputs. Therefore, it is interesting to exploit the multifunctionality and tunability of spin-torque to imitate the sharp neuron spikes.

Here, we propose a simple way to imitate neuron spiking in high-magnetoresistance nanoscale spin valves where both magnetic layers are free and thin enough to be switched through spin torque [16–18]. We study these devices through macrospin and micromagnetic simulations [19]. We show that the windmill motion induced by spin torque [20] in these structures gives rise to spikes whose shape and frequency, set by the charging and discharging times, can be tuned through the amplitude of injected dc current as well as the materials and thicknesses of the ferromagnetic layers. We observe that these devices with many coupled degrees of freedom can exhibit chaotic oscillations. In our paper, "chaos" means the dynamics whose behavior after a long period of time is unpredictable because of the sensitivity to initial conditions, although the behavior is determined by

*rie-matsumoto@aist.go.jp

scientific laws or equations [in our case, Eqs. (1) and (2)] [21]. The time evolution of the magnetization direction is deterministic, but it is difficult to predict the direction after a long period of time. Only after the numerical simulations with the equations does the magnetization direction become predictable. On the other hand, the noisy dynamics is not deterministic because of its stochastic behavior.

Chaoticlike neuron dynamics has been observed in the brain and dynamics at the edge of chaos has been considered to optimize information processing [15,22,23]. In this paper, the term "chaoticlike" dynamics indicates the dynamics at the edge of chaos or at a critical point, i.e., dynamics between ordered dynamics and chaotic dynamics [23]. It is predicted by the "criticality hypothesis" that neural networks will self-organize to operate near a critical point that is close to the chaotic regime [15,22,23]. This phenomenon is called self-organized criticality. Self-organized criticality is often pointed out in network chaos and the degree of chaos in a neural network should depend on the degree of chaos in a single neuron.

We point out that the dipolar coupling between magnetic layers is the main source of chaos in spin-torque windmill relaxation oscillators. We demonstrate that the degree of chaos can be tuned in a wide range by engineering the magnetic stack and anisotropies. The proposed spiking windmill spin-torque relaxation oscillator with controllable chaos is a promising building block for hardware neuromorphic chips, leveraging nonlinear dynamics for computing.

Disordered dynamics is desirable in some neuromorphic computing applications [24–31]. For example, in recurrent neural networks, the information processing capacity is maximized at the edge of chaos [24,25]. The disordered spiking oscillators in the scheme of the array enhanced stochastic resonance (AESR) can be useful for faint-signal detection and phase-locked loops [27–30]. In this scheme, noises composed of multiple frequencies enhance the ability for the signal detection and transmission [29,30]. Its sensitivity is higher in the network where each oscillator is equipped with an individual noise source than in the network where the oscillators are exposed to a common noise source [28]. The disordered spiking dynamics we propose can be used as an internal noise source. Also, the sensitivity is maximized by tuning the amount of noise and/or the number of the oscillators [27–30]. Even in the case of a single neuron, disordered spiking dynamics can be beneficial to the faithful transmission of high-frequency inputs, although it requires analysis using many cycles of the inputs [31]. On the other hand, chaotic and chaoticlike dynamics should be avoided in other neuromorphic computing applications [32]. The above-mentioned facts supports the importance of being able to tune the degree of chaos in a system.

II. WINDMILL RELAXATION OSCILLATIONS: PRINCIPLE

The structure of the proposed windmill relaxation oscillator, illustrated in Fig. 1(a), is a spin valve, consisting of a nonmagnetic spacer layer sandwiched between two ferromagnetic layers. The spacer layer can be either a metallic layer in giant magnetoresistance devices [33,34] or a thin insulating tunnel barrier layer in magnetic tunnel junctions [35–39]. The two magnetizations, $\boldsymbol{m}_1$ and $\boldsymbol{m}_2$, have preferential directions due to magnetic anisotropy. However, contrary to typical spin-valve stacks, both layers are free to switch: neither of them is pinned. In the absence of spin torque, the magnetization directions are either parallel (P) or antiparallel (AP). They can point in-plane (IP) [40] or out-of-plane (OOP) [41], depending on the dominant source of anisotropy. When a dc current is injected in the spin valve, perpendicularly to the layer planes, the torques on the two magnetizations tend to induce rotations in the same direction, as illustrated in Fig. 1(b). The direction of rotation is set by the sign of the applied dc current.

III. MODEL

It has been predicted, as well as experimentally observed, that this torque configuration can generate a windmill-like motion of the two magnetizations [16–18,20]. The equations of motion of the magnetizations are given by the Landau-Lifschitz-Gilbert-Slonczewski (LLGS) equation [9,10,42]:

$$\frac{\partial \hat{\boldsymbol{m}}_1}{\partial t} = -\gamma \hat{\boldsymbol{m}}_1 \times \boldsymbol{H}_{\text{eff1}} + \alpha \hat{\boldsymbol{m}}_1 \times \frac{\partial \hat{\boldsymbol{m}}_1}{\partial t} - \gamma \tau_{\text{st1}} \hat{\boldsymbol{m}}_1 \times (\hat{\boldsymbol{m}}_1 \times \hat{\boldsymbol{m}}_2), \quad (1)$$

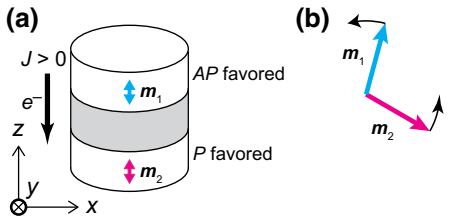

FIG. 1. (a) Schematic of the spin-torque windmill spiking oscillator: a spin valve with two free layers. The double-headed arrow in cyan (magenta) represents the magnetization unit vector, $\boldsymbol{m}_1$ ($\boldsymbol{m}_2$), in the equilibrium states. The axis z is parallel to the OOP direction. When the current density (J) is positive, electrons (e^-) flow from $\boldsymbol{m}_1$ to $\boldsymbol{m}_2$. (b) Schematic of the windmill spin-torque configuration of the two magnetizations $\boldsymbol{m}_1$ and $\boldsymbol{m}_2$. In the case of $J > 0$, $\boldsymbol{m}_1$ switches away from $\boldsymbol{m}_2$, and $\boldsymbol{m}_2$ follows $\boldsymbol{m}_1$ as indicated by the arrows. In other words, at $J > 0$, $\boldsymbol{m}_1$ favors an antiparallel (AP) configuration and $\boldsymbol{m}_2$ favors a parallel (P) configuration, as indicated in (a).

$$\frac{\partial \hat{\boldsymbol{m}}_2}{\partial t} = -\gamma \hat{\boldsymbol{m}}_2 \times \boldsymbol{H}_{\text{eff2}} + \alpha \hat{\boldsymbol{m}}_2 \times \frac{\partial \hat{\boldsymbol{m}}_2}{\partial t} + \gamma \tau_{\text{st2}} \hat{\boldsymbol{m}}_2 \times (\hat{\boldsymbol{m}}_2 \times \hat{\boldsymbol{m}}_1). \quad (2)$$

Here, t and γ are the time and the electron gyromagnetic ratio. The second term on the right-hand side of Eqs. (1) and (2) is the damping-torque term, where α is the Gilbert damping constant. In this article, $\alpha = 0.01$ is assumed. Hereafter, i in the subscript represents the quantities of the layer having $\boldsymbol{m}_i$ layer where $i = 1$ or 2. τ_{st1} and τ_{st2} represent the coefficient of the Slonczewski torque:

$$\tau_{\text{st}i} = \frac{\hbar}{2} \frac{1}{\mu_0 M_s} \frac{1}{d_i} \frac{J}{|e|} P. \quad (3)$$

Here, $\hbar$ is the Dirac constant, μ_0 is the vacuum permeability, M_s is the saturation magnetization, d_i is the thickness of layer i, e is the electron charge, J is the current density, and P is the spin polarization. In the rest of the paper, we take $P = 0.6$. $\boldsymbol{H}_{\text{eff}i}$ is the effective field, expressed as

$$\boldsymbol{H}_{\text{eff}} = \boldsymbol{H}_{\text{anis}} + \boldsymbol{H}_{\text{dip}}. \quad (4)$$

Hereafter, the layer index, i, is abbreviated. $\boldsymbol{H}_{\text{anis}}$ represents the anisotropy field, expressed as

$$\boldsymbol{H}_{\text{anis}} = \frac{2K}{\mu_0 M_s} m_z. \quad (5)$$

Here, K represents the anisotropy constant. In the spin valve shown in Fig. 1(a), $K = 115$ kJ/m^3 is assumed in $\boldsymbol{m}_1$, and $K = 70$ kJ/m^3 is assumed in $\boldsymbol{m}_2$. $\boldsymbol{H}_{\text{dip}}$ represents the dipolar field, expressed as

$$\boldsymbol{H}_{\text{dip}} = -M_s \left(N_x m_x, N_y m_y, N_z m_z\right). \quad (6)$$

Here, N_x, N_y, and N_z are the demagnetization coefficients [43].

IV. RESULTS

To highlight the principle of windmill relaxation oscillator, we first neglect the dipolar-field interactions between the two magnetic layers in Fig. 1(a) and consider that they behave as macrospins with uniform magnetizations. Figure 2(a) shows macrospin simulations of magnetic switching in these conditions, for out-of-plane magnetized layers that differ only through their anisotropy constants: $K_{\boldsymbol{m}_1} = 115$ kJ/m^3 and $K_{\boldsymbol{m}_2} = 70$ kJ/m^3 (the other magnetic parameters are indicated as SV_{OOP1} in Table I). The windmill motion induces sustained switching of the magnetizations one after the other at $J \geq J_{\text{th}} = 1.0$ MA/cm^2, where J_{th} is the threshold current density for sustained windmill switching. The repeated magnetic switches give rise to changes in the device resistance (R) through magnetoresistance (MR) effects: $R = (R_{\text{AP}} + R_{\text{P}})/2 - [(R_{\text{AP}} - R_{\text{P}})/2] \cos \hat{\theta}_{12}$, where R_{P} (R_{AP}) is the resistance in the parallel (antiparallel) configuration and $\hat{\theta}_{12}$ is the angle between $\boldsymbol{m}_1$ and $\boldsymbol{m}_2$. Since the injected current is dc, the resulting voltage variations across the spin valve, i.e., $V = R \times I_{\text{dc}}$, are proportional to the resistance variations. In this paper, we always consider a MR ratio $(R_{\text{AP}} - R_{\text{P}})/R_{\text{P}}$ of 100% and $R_{\text{P}} = 100\ \Omega$, assuming that spin valves are magnetic tunnel junctions. The resistance variations corresponding to the magnetic switches in Fig. 2(a) are plotted in Fig. 2(b). A spiking behavior similar to neuron responses is observed. The low-resistance states just after spikes correspond to the refractory periods. At the low-resistance states where $R \sim R_{\text{P}} = 100\ \Omega$, $\hat{\theta}_{12} \sim 0°$. $\hat{\theta}_{12}$ gives the spin-torque strength, which is proportional to $|\sin \hat{\theta}_{12}|$. The spin-torque strength is zero at $\hat{\theta}_{12} = 0°$ and 180°. Thus, at $\hat{\theta}_{12} \sim 0°$, magnetizations hardly move. The time scales of these relaxation oscillations are set by the switching times of the two layers. Here, the long charging period corresponds to the switching of $\boldsymbol{m}_1$ and the short discharge period to the switching of $\boldsymbol{m}_2$. At $|J| < |J_{\text{th}}|$, on the other hand, no spike appears in the resistance time trace.

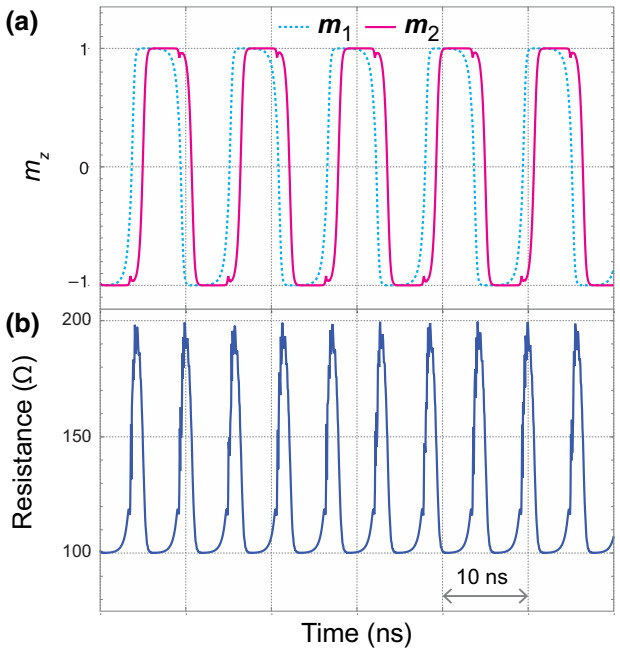

FIG. 2. (a) Times traces of magnetization switching (macrospin simulations for a spin valve with OOP magnetized layers without dipolar-field interaction between the two ferromagnetic layers, SV_{OOP1}) (b) Corresponding resistance time trace. In (a) and (b), J is positive and the normalized current density is $J/J_{\text{th}} = 1.5$.

The asymmetry of the switching times comes from the different anisotropy constants of the layers used in the simulations ($K_{\boldsymbol{m}_1} = 115$ kJ/m^3 and $K_{\boldsymbol{m}_2} = 70$ kJ/m^3). Indeed, the magnetization switching time T_{SW} under spin torque is

TABLE I. Structures under study (SV_{OOP1}, SV_{OOP2}, SV_{IP1}, SV_{IP2}, and SV_{IP3}); simulation method; and threshold current density (J_{th}). m_{A1}, m1, m2 and m_{A2} represent the magnetic layers which have magnetization $\boldsymbol{m}_{A1}$, $\boldsymbol{m}_1$, $\boldsymbol{m}_2$ and $\boldsymbol{m}_{A2}$, respectively. OOP1, OOP2, IP1, IP2 are the labels of magnetic layers whose parameters are summarized in Table II. In all structures, the spacer layer between m1 and m2 has the thickness of 1 nm and its $J_{RKKY} = 0$. In (d) SV_{IP2}, the spacer layer between m1 and m_{A1} (m2 and m_{A2}) has the thickness of 0.7 nm and its $J_{RKKY} = -0.1$ mJ/m^2.

Structure	(a) SV_{OOP1}	(b) SV_{OOP2}	(c) SV_{IP1}	(d) SV_{IP2}	(e) SV_{IP3}
m_{A1}	...	...	...	IP1	...
m1	OOP1	OOP1	IP1	IP1	IP1
m2	OOP2	OOP2	IP2	IP2	IP2
m_{A2}	...	...	...	IP2	...
Simulation method	Macrospin[a]	Micromagnetics[b]	Macrospin[a]	Micromagnetics[b]	Micromagnetics[b]
$J_{th}(>0)$ (MA/cm^2)	1.0	1.1	...[c]	21	...[c]
$J_{th}(<0)$ (MA/cm^2)	−1.0	−1.1	−6.0	−23	−34

[a]Macrospin-model simulations were conducted without dipolar coupling.
[b]Micromagnetic simulations were conducted with dipolar coupling.
[c]In (c) SV_{IP1} and (e) SV_{IP3}, positive current induces continuous spin-torque oscillations of $\boldsymbol{m}_1$ and $\boldsymbol{m}_2$, which does not result in a spiking time trace of resistance.

proportional to $1/(J - J_{th}^{(0)})$ [44], where $J_{th}^{(0)}$ is the individual threshold current density for switching [17]. Layers with higher anisotropy K are more difficult to switch and have a larger threshold current density $J_{th}^{(0)}$. In our case, we find through simulations that $J_{th1}^{(0)}$ and $J_{th2}^{(0)}$ are respectively equal to 0.95 MA/cm^2 and 0.49 MA/cm^2, where $\boldsymbol{m}_2$ ($\boldsymbol{m}_1$) is fixed at the equilibrium state during the evaluation of $J_{th1}^{(0)}$ ($J_{th2}^{(0)}$). The switching times during the windmill motion for the two magnetic layers as a function of current density are plotted in Fig. 3(a) (solid curves), together with the corresponding fits in $T_{SWi} = c_i/(J - J'_{thi})$ (dotted curve and dotted-dashed curve). Here, c_i and J'_{thi} are fitting parameters. The agreement between the analytical prediction of Ref. [44] and our simulations is excellent. The fitting yields $J'_{th1} = 0.954 \pm 0.002$ MA/cm^2, $c_1 = 4.088 \pm 0.215$ ns MA/cm^2, $J'_{th2} = 0.471 \pm 0.015$ MA/cm^2, and $c_2 = 1.305 \pm 0.031$ ns MA/cm^2. The threshold currents extracted from the switching times J'_{th1} (J'_{th2}) agree well with the previously determined threshold currents $J_{th1}^{(0)}$ ($J_{th2}^{(0)}$). These results show that the response of the windmill relaxation oscillator can be tuned by dc current. Traces at different dc current densities are shown in Fig. 3(b), and the evolution of the frequency as a function of current is plotted in Fig. 3(c). As determined experimentally and numerically in previous studies [16–18], the frequency increases with an increase of $|J|$. Note that the shape of spikes can also be tuned by controlling the switching time ratio through materials engineering of the two layers (M_s, P, etc.). Figure 3(b) shows reversed spikes at negative current density. This feature can allow coupling relaxation oscillators in both an excitatory and inhibitory way using adder circuits for the summation of input signals. Another way of excitatory and inhibitory coupling is to use synaptic connections. By adjusting the resistance of a memristive device that corresponds to synaptic weights, the coupling of spiking oscillators can be tuned [45,46].

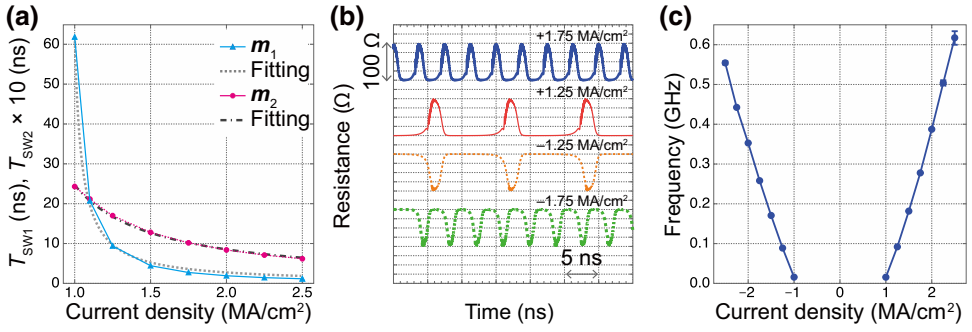

FIG. 3. (a) Average switching times (T_{SW1} and T_{SW2}) for $\boldsymbol{m}_1$ (solid triangles on solid curve) and $\boldsymbol{m}_2$ (solid circles on solid curve) as a function of current density, with fits by $c_i/(J - J'_{thi})$ (dotted curve and dotted-dashed curve). (b) Resistance time traces at $J = +1.75$ MA/cm^2 (thick solid curve), $+1.25$ MA/cm^2 (thin solid curve), -1.25 MA/cm^2 (thin dotted curve), -1.75 MA/cm^2 (thick dotted curve). (c) Frequency as a function of current density for negative and positive current densities.

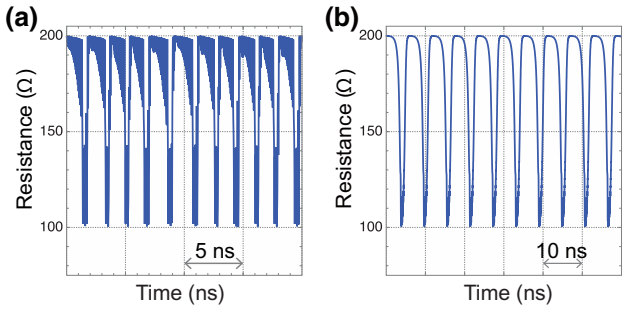

FIG. 4. Resistance time traces for (a) in-plane and (b) out-of-plane magnetized layers at negative J with $J/J_{\rm th} = 1.5$.

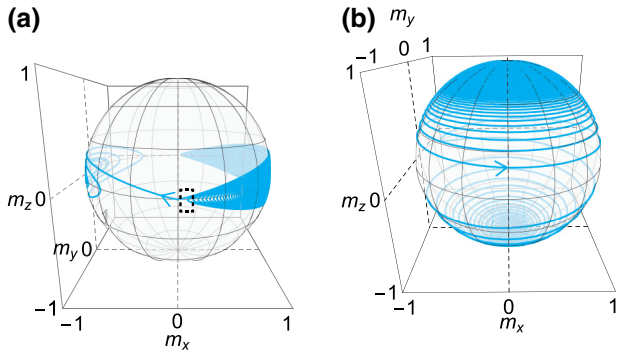

FIG. 5. Sketch of magnetization orbits of $\boldsymbol{m}_1$ for (a) in-plane and (b) out-of-plane magnetized layers at negative $J_{\rm th}$.

V. OCCURRENCE OF CHAOS

Figure 4 compares resistance versus time traces simulated through macrospin equations of motion for in-plane [Fig. 4(a)] and out-of-plane magnetized spin valves [Fig. 4(b)] [the structure of the in-plane magnetized spin valve, $\mathrm{SV_{IP1}}$, and its parameters are shown in Fig. 6(c) and Tables I and II]. As can be seen, the trace in the out-of-plane case is highly regular, whereas fluctuations affect the periodicity of switching in the in-plane case, even if temperature-induced fluctuations are not included in the simulations. The reduced periodicity, that is, the presence of chaos in $\mathrm{SV_{IP1}}$, will be more clearly seen in the quantitative analyses shown in Table III of Sec. VI.

This chaotic switching of in-plane spin valves [47] under windmill motion can be interpreted in the following way. For windmill motion, the switching of one layer toggles the switching of the other. Indeed, magnetization $\boldsymbol{m}_1$ wants to achieve the AP configuration, whereas $\boldsymbol{m}_2$ wants to maintain a P configuration (and inversely for a reversed sign of the current density); therefore, the P and AP configurations become consecutively unstable. However, the switching trajectories are very different for in-plane and out-of-plane magnetized samples.

As shown in Fig. 5(a), for in-plane magnetized samples, the strong anisotropy distorts the trajectories in a clamshell shape. During the dynamics, the spin torque competes with the damping torque, which makes magnetizations relax to the direction of $\boldsymbol{H}_{\rm eff}$ while dissipating magnetic energy. In in-plane magnetized samples, the damping torque makes the magnetization relax to (m_x, m_y, m_z)=$(\pm 1, 0, 0)$ when spin torque is zero. Larger spin torque makes the clamshell trajectory larger, but the energy dissipation by the damping torque becomes larger at a larger trajectory [42]. When the trajectory reaches the bifurcation points at (m_x, m_y, m_z)=$(0, \pm 1, 0)$, the magnetization can switch.

Let us consider the situation where one of the magnetizations, $\boldsymbol{m}_2$, is close to equilibrium and the other one, $\boldsymbol{m}_1$, is switching toward $\boldsymbol{m}_2$. The switching of $\boldsymbol{m}_1$ from one hemisphere to the other is strongly determined by the exact magnetization dynamics in the narrow window highlighted in Fig. 5(a). In this dotted window, the angle between magnetizations $\hat{\theta}_{12}$ that gives the torque strength is also strongly varying. The spin-torque strength is proportional to $|\sin\hat{\theta}_{12}|$. It is zero at $\hat{\theta}_{12} = 0^\circ$ and 180° and maximized at $\hat{\theta}_{12} = 90^\circ$. The closer to 90° $\hat{\theta}_{12}$ is, the easier becomes the switching of $\boldsymbol{m}_1$ from the dotted window. Therefore, small variations in the direction of $\boldsymbol{m}_2$ strongly influence the switching of $\boldsymbol{m}_1$. This high coupling between degrees of freedom induces a high sensitivity of magnetization reversal to initial conditions and can favor the appearance of chaos.

The situation is different for out-of-plane magnetized samples. Here, the competition between spin torque and damping torque is most severe at $(m_x, m_y, m_z) = (0, 0, \pm 1)$ [48]. Once $\boldsymbol{m}_1$ deviates from $(0, 0, \pm 1)$, precessions of $\boldsymbol{m}_1$ remain mostly circular during the whole switching of $\boldsymbol{m}_1$ [Fig. 5(b)]. Therefore, precessions are much less sensitive to fluctuations of $\boldsymbol{m}_2$.

Until now, we have not included the dipolar-field interaction between the magnetic layers in the simulations. The dipolar-field interaction is expected to enhance strongly the chaoticity of the system because it increases the coupled degrees of freedom. Indeed, if the dipolar-field interaction

TABLE II. Parameters of magnetic layers: OOP1, OOP2, IP1, and IP2. S is the area of the base.

Magnetic layer	OOP1	OOP2	IP1	IP2
S (nm^2)	$16 \times 16 \times \pi$	$16 \times 16 \times \pi$	$30 \times 10 \times \pi$	$30 \times 10 \times \pi$
d (nm)	1	1	1	0.5
M_s (kA/m)	200	200	1300	1300
K (kA/m^3)	115	70	0	0

TABLE III. Evaluated degree of chaos: quality factor (Q factor), [*DET*, L, $L_{\max}$, *ENTR*] of Recurrence Quantification Analysis (RQA), and Lyapunov exponent of SV_{OOP1}, SV_{OOP2}, SV_{IP1}, SV_{IP2}, and SV_{IP3} at $J/J_{th} = 1.5$.

Method	(a) SV_{OOP1}	(b) SV_{OOP2}	(c) SV_{IP1}	(d) SV_{IP2}	(e) SV_{IP3}
Q factor	$> 10^4$	440	11	2.5	3.7
DET(%)	0.88	0.66	0.10	0.066	0.11
L	5.4	4.5	2.4	2.2	2.3
$L_{\max}$	3100	650	40	8	9
ENTR	1.9	1.7	0.81	0.44	0.69
Lyapunov exponent (Gbit/s)	0.14	0.89	4.5	5.0	6.9

exists, the switching of $\boldsymbol{m}_2$ will strongly depend on the direction of $\boldsymbol{m}_1$ (and reciprocally), yielding an increased sensitivity of the repeated magnetization switching events on initial conditions.

VI. TUNING CHAOS BY STRUCTURE

The strength of the dipolar-field interaction between layers (dipolar coupling) can be controlled by tuning the anisotropy and by tuning the stack. In this section, we compare the windmill dynamics in the different structures sketched in Fig. 6.

Figure 6(a) shows an out-of-plane bilayer macrospin spin valve simulated without dipolar-field interaction (SV_{OOP1}). The dipolar-field interaction is included in the micromagnetic simulations of the out-of-plane bilayer (SV_{OOP2}) of Fig. 6(b) (micromagnetic simulations are described in the Appendix). However, the dipolar-field interaction in the out-of-plane configuration is expected to be small because of the small M_s. Figure 6(c) shows an in-plane bilayer macrospin spin valve without the dipolar-field interaction (SV_{IP1}). Figure 6(d) shows a structure with a more complicated stack, where the free layers are each composed of two antiferromagnetically coupled layers (SV_{IP2}). The dipolar field between the two free layers is expected to be strongly minimized in this configuration thanks to flux closure. Finally, Fig. 6(e) shows an in-plane bilayer spin valve (SV_{IP3}), including the dipolar-field interaction, which is expected to be strong in this configuration. Because of the dipolar-field interaction, SV_{IP3} favors AP magnetization configuration. As a result, the switching from the AP to the P configuration is often interrupted and the resistance oscillates in a higher range around 150–200 Ω.

Typical time traces are shown below each structure. As can be seen, the degree of chaos seems to increase when the anisotropy changes from out-of-plane [Figs. 6(a) and 6(b)] to in-plane [Fig. 6(c)]. It also increases in the in-plane configuration when the strength of dipolar-interaction between layers increases [Figs. 6(c)–6(e)].

In order to evaluate more thoroughly the degree of chaos in structures shown in Fig. 6, we have used three methods: quality factor (Q factor), recurrence quantification analysis (RQA) [49–52], and Lyapunov exponent [53]. Low Q factor and low *DET*, L, $L_{\max}$ and *ENTR* in RQA indicate a high degree of chaos, and a high Lyapunov exponent indicates a high degree of chaos. Here, *DET* is Determinism being the percentage of recurrence points which form diagonal lines, L is averaged diagonal line length, $L_{\max}$ is the length of the longest diagonal line, and *ENTR* is Entropy being the Shannon entropy of the probability distribution of the diagonal line lengths. The evaluated values at $J/J_{th} = 1.5$ are summarized in Table III.

First, we have extracted a quality factor (Q factor) for the interspike time interval from each time trace. In Figs. 6(a), 6(b), and 6(d) [Figs. 6(c) and 6(e)], each time interval where $R \leq 150\ \Omega$ ($R \geq 150\ \Omega$) is defined as the interspike time interval. The Q factor is evaluated as T_I/σ_I during 10 sets of switching of $\boldsymbol{m}_1$ and $\boldsymbol{m}_2$, where T_I (σ_I) is the average value (standard deviation) of interspike time interval. As we see the enhanced chaotic magnetization dynamics in the in-plane magnetized spin valve in Sec. V, the Q factor decreases when the anisotropy changes from out-of-plane [(a) SV_{OOP1} and (b) SV_{OOP2}] to in-plane [(c) SV_{IP1}, (d) SV_{IP2}, and (e) SV_{IP3}]. In (a) SV_{OOP1}, the Q factor exceeds our analyzable upper limit of 10^4 because $\sigma_I = 0$ in our simulation with a time step of 1 ps. The Q factor also decreases by the introduction of dipolar-field interaction between layers [(a) SV_{OOP1} versus (b) SV_{OOP2} and (c) SV_{IP1} versus (d) SV_{IP2} and (e) SV_{IP3}]. However, the flux-closure structure in Fig. 6(d) hardly improves the Q factor. Nevertheless, it recovers the full amplitude of resistance oscillation compared to Fig. 6(e) and reduces the threshold current J_{th}.

Then we have conducted recurrence quantification analysis of $R(t)$ for each structure. Recurrence plots for each structure are shown at the bottom of Fig. 6. A recurrence plot [49,50] is a square matrix, in which the matrix elements correspond to those times at which a similar resistance state recurs, i.e., a plot of $\Re_{\iota,\kappa} = \Theta(\epsilon_\iota - \|R(t_\iota) - R(t_\kappa)\|)$. Here, t_ι and t_κ are time during about 10 periods of resistance oscillation shown in the middle panels of Fig. 6. ϵ_ι is a threshold distance and $\epsilon_\iota = 0.05\ \Omega$ is chosen in Fig. 6. Θ is the Heaviside function, and the elements where $\Re_{\iota,\kappa} = 1$ are dots in the recurrence plots. In other words, the elements where $R(t_\iota) \sim R(t_\kappa)$ appear as dots in the plots. Trivial dots at the matrix diagonal elements at $t_\iota = t_\kappa$ are removed. A perfectly periodic oscillator has dots

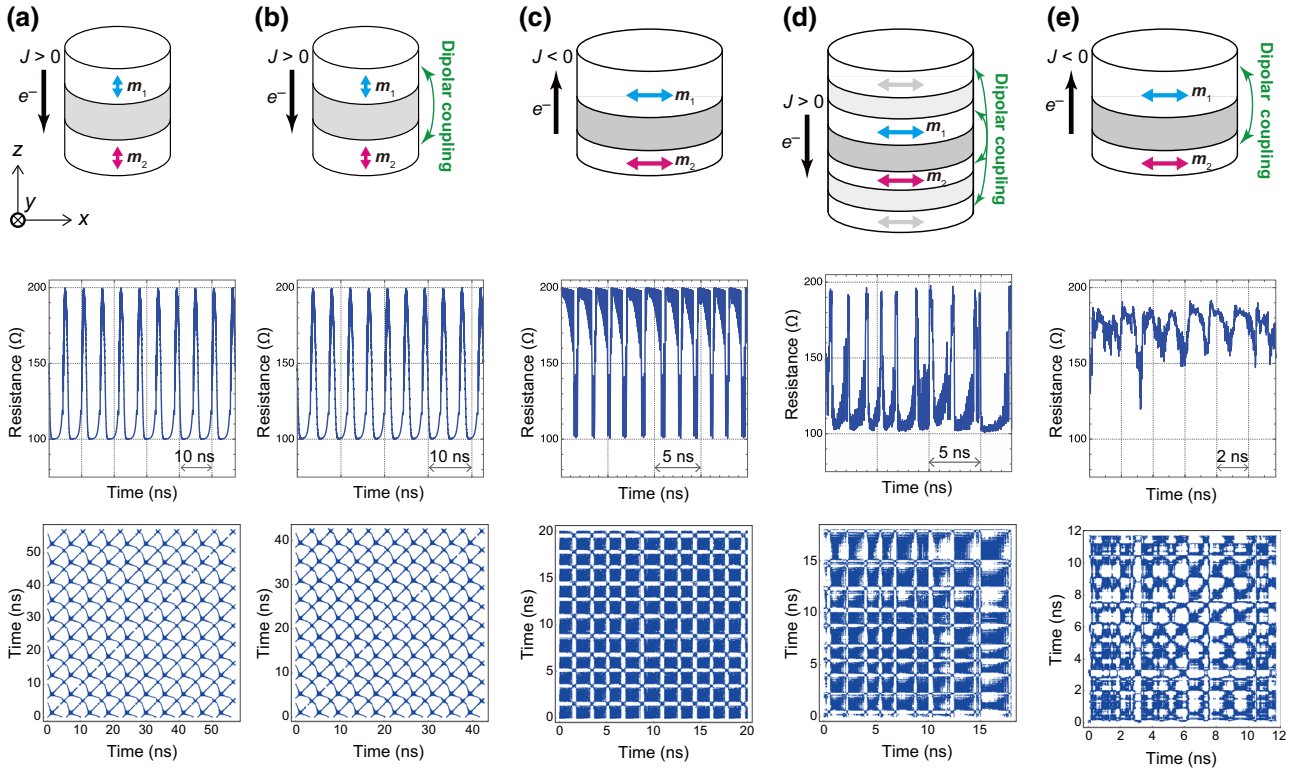

FIG. 6. Sketch of the different structures: (a) macrospin OOP spin valve without dipolar coupling (SV_{OOP1}), (b) micromagnetic OOP spin valve with dipolar coupling (SV_{OOP2}), (c) macrospin IP spin valve without dipolar coupling (SV_{IP1}), (d) micromagnetic IP spin valve with antiferromagnetically coupled layers (m_{A1} and m_{A2}) and with dipolar coupling (SV_{IP2}), (e) micromagnetic IP spin valve with dipolar coupling (SV_{IP3}). The x (z) axis is parallel to the major axis of the ellipse (out-of-plane direction). Typical traces of the resistance versus time and the corresponding recurrence plots are shown below each case for $J/J_{th} = 1.5$.

mainly along the diagonal. In Figs. 6(d) and 6(e), the plots show patterns with reduced regularity reflecting their high degree of chaos compared to the cases of Figs. 6(a)–6(c). Results of recurrence quantification analysis [50–52], i.e., *DET*, *L*, L_{max}, and *ENTR*, are summarized in the middle of Table III. *DET*, *L*, L_{max}, and *ENTR* are quantities characterized by the diagonal lines in a recurrence plot. The lengths of diagonal lines are directly related to the ratio of predictability inherent to the system. Suppose that the states at times t_ι and t_κ are neighboring. If the system exhibits predictable behavior, similar situations will lead to a similar future; i.e., the probability for $R(t_\iota + \delta t) \sim R(t_\kappa + \delta t)$ is high. For perfectly periodic systems, this result leads to infinitely long diagonal lines. In contrast, if the system is chaotic, the probability for $R(t_\iota + \delta t) \sim R(t_\kappa + \delta t)$ is small and we only find single points or short lines. In accordance with the evaluated Q factors, *DET*, *L*, L_{max}, and *ENTR* decrease when the anisotropy changes from out-of-plane to in-plane. They also decrease by the introduction of dipolar interaction between layers.

Then we have determined the Lyapunov exponent from each time trace [53]. The Lyapunov exponent is a quantity that characterizes the rate of separation of infinitesimally close trajectories in dynamic systems. Lyapunov exponents are evaluated with about 100 periods of resistance oscillation for each structure. As we expected, the Lyapunov exponent, characterizing the degree of chaos, increases when the anisotropy changes from out-of-plane to in-plane. It also increases in the in-plane configuration when the strength of dipolar interaction between layers increases. These results show that the degree of chaos can be tuned in a wide range by engineering the magnetic stack and anisotropies, which is suitable for various neuromorphic computing applications.

VII. TUNING CHAOS BY CURRENT

We also checked the tunability of chaos by current. The evaluated current density dependence of quality factors (Q factors) and Lyapunov exponents is shown in Fig. 7. $J/|J_{th}|$ represents the current density normalized by the threshold current density for each polarity of current. The Lyapunov exponents at $J/|J_{th}| = \pm 1$ are not shown because the too long interspike time interval against pulse width makes evaluation of the Lyapunov exponent itself impossible and long simulations of 100 periods are not possible with our computational capacity. Both trends in Figs. 7(a) and 7(b) show that the degree of chaos is

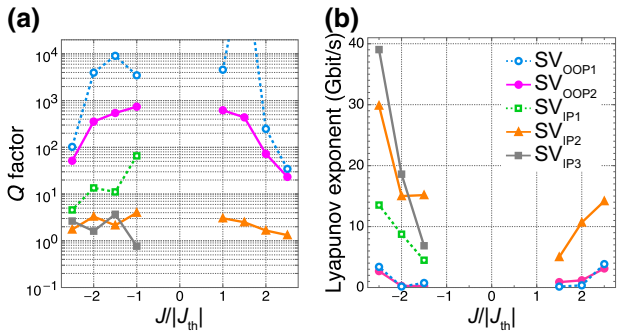

FIG. 7. (a) $J/|J_{\rm th}|$ dependence of the Q factor of the interspike time interval and (b) Lyapunov exponent. Open circles on dotted lines are for $\mathrm{SV_{OOP1}}$. Solid circles on solid lines are for $\mathrm{SV_{OOP2}}$. Open squares on dotted lines are for $\mathrm{SV_{IP1}}$. Solid triangles on solid lines are for $\mathrm{SV_{IP2}}$. Solid squares on solid lines are for $\mathrm{SV_{IP3}}$.

increased by increasing the magnitude of $J/|J_{\rm th}|$. One might notice the deviation from the trend in $\mathrm{SV_{OOP1}}$, $\mathrm{SV_{IP2}}$, and $\mathrm{SV_{IP3}}$, whose degrees of chaos at small $|J/J_{\rm th}|$ are larger than those at medium $J/|J_{\rm th}|$. At small $|J/J_{\rm th}|$, that is, around ± 1, just after the switching of $\boldsymbol{m}_1$ or $\boldsymbol{m}_2$, an almost complete P or AP configuration is made. Around $\hat{\theta}_{12} \sim 0^\circ$ and 180°, the spin-torque strength, which is proportional to $|\sin\hat{\theta}_{12}|$, is approximately 0, but it is very sensitive to $\hat{\theta}_{12}$. The small difference of $\hat{\theta}_{12}$ just after switching of $\boldsymbol{m}_1$ (or $\boldsymbol{m}_2$), results in a large difference in switching time of $\boldsymbol{m}_2$ (or $\boldsymbol{m}_1$). Therefore, the deviation from the trend occurs at small $|J/J_{\rm th}|$. A cause of the increased degree of chaos at large $|J/J_{\rm th}|$ can be the increased instability of $\boldsymbol{m}_2$ during the interspike time interval. Fluctuations of $\boldsymbol{m}_2$ strongly vary the angle between magnetizations $\hat{\theta}_{12}$, which gives the torque strength. Therefore, the switching of $\boldsymbol{m}_1$ is complex through the dynamics of $\boldsymbol{m}_2$. The trend in Fig. 7 means that the degree of chaos can be tuned in a wide range by the dc current. The tunability of chaos by the current is quite beneficial because it enables the control of chaos in real time in a ready-made circuit.

VIII. TOWARD SPINTRONIC NEURONS

In this paper, we propose spintronic relaxation oscillators that show spiking dynamics whose degree of chaos can be tuned by structures and current. In order for the spintronic relaxation oscillators to be used as hardware neurons in applications, they should be equipped with functions such as temporal coding and excitability [54] and an ability to synchronize with other spintronic relaxation oscillators [45,46]. They should also ensure high fan-out and fan-in. In the case of spintronic relaxation oscillators, they can couple with each other through couplings other than electronic connections, which require wires. For example, spintronic relaxation oscillations can be coupled through dipolar couplings, through spin waves, and through microwaves [55,56]. Because these couplings do not require electrical wires, spintronic relaxation oscillators can be advantageous for ensuring high fan-out and fan-in.

IX. CONCLUSION

We propose a simple way to imitate neuron spiking in high-magnetoresistance nanoscale spin valves where both magnetic layers are free and can be switched by spin torque. Our numerical-simulation results show that the windmill motion induced by spin torque in the proposed spintronic relaxation oscillators gives rise to spikes whose shape and frequency can be tuned through the amplitude of injected dc current. We also find that these devices can exhibit chaotic oscillations. By evaluating the quality factors of interspike time intervals and Lyapunov exponents, as well as conducting recurrence quantification analysis for the time evolutions of resistance, we demonstrate that the degree of chaos can be tuned in a wide range by engineering the magnetic stack and anisotropies and by changing the dc current. The degree of chaos increases when the anisotropy of the free layer changes from out-of-plane to in-plane. It also increases when the dipolar-field interaction between the free layers increases. The proposed spintronic relaxation oscillator is a promising building block for hardware neuromorphic chips leveraging complex nonlinear dynamics for computing.

ACKNOWLEDGMENTS

This work was partly supported by JSPS KAKENHI Grant No. JP16K17509 and JP19K05259 and the European Research Council (ERC) under Grant No. bioSPINspired 682955.

APPENDIX: MODEL IN MICROMAGNETIC SIMULATIONS

In micromagnetic simulations, $\hat{\boldsymbol{m}}_i = (m_{xi}, m_{yi}, m_{zi})$ of Eqs. (1) and (2) means the unit magnetization vector of a unit cell at the position $\boldsymbol{r}_i$, $\hat{\boldsymbol{m}}_i(\boldsymbol{r}_i)$. The simulations are conducted with the simulation code SPINPM [19]. In the micromagnetic simulations of this paper, each magnetic layer is divided into unit cells with the area of 4×4 nm. In the third term on the right side of Eqs. (1) and (2), i.e., the Slonczewski-torque term, the x and y components of $\boldsymbol{r}_1$ and $\boldsymbol{r}_2$ are the same.

In Eqs. (1) and (2), $\boldsymbol{H}_{\rm eff}$ is the effective field, expressed as

$$\boldsymbol{H}_{\rm eff} = \boldsymbol{H}_{\rm exch} + \boldsymbol{H}_{\rm anis} + \boldsymbol{H}_{\rm dip} + \boldsymbol{H}_{\rm RKKY}. \tag{A1}$$

$\boldsymbol{H}_{\rm exch}$ represents the exchange field, expressed as

$$\boldsymbol{H}_{\rm exch} = \frac{2A}{\mu_0 M_s}\nabla^2\hat{\boldsymbol{m}}. \tag{A2}$$

A is the exchange constant. In the micromagnetic simulations, it is assumed to be $A = 2 \times 10^{-11}$ J/m in this paper. Note that $\hat{\boldsymbol{m}}$ in Eqs. (A2) and (A3) represents $\hat{\boldsymbol{m}}_i$ or $\hat{\boldsymbol{m}}_{\mathrm{A}_i}$. $\boldsymbol{H}_{\mathrm{dip}}$ represents the dipolar field. $\boldsymbol{H}_{\mathrm{dip}}$ on the position $\boldsymbol{r}$ is expressed as

$$\boldsymbol{H}_{\mathrm{dip}} = -\frac{M_s}{4\pi}\int_{\mathrm{Vol}}\left[\frac{\hat{\boldsymbol{m}}(\boldsymbol{r}')}{|\boldsymbol{r}-\boldsymbol{r}'|^3} - \frac{3[\hat{\boldsymbol{m}}(\boldsymbol{r}')\cdot(\boldsymbol{r}-\boldsymbol{r}')]}{|\boldsymbol{r}-\boldsymbol{r}'|^5}(\boldsymbol{r}-\boldsymbol{r}')\right]d\boldsymbol{r}'. \tag{A3}$$

Here, the integral is performed over the volume (Vol) including all magnetic layers. $\boldsymbol{H}_{\mathrm{RKKY}}$ represents the RKKY coupling field, expressed as

$$\boldsymbol{H}_{\mathrm{RKKY}} = \frac{J_{\mathrm{RKKY}}}{\mu_0 M_s d}\nabla\left(\hat{\boldsymbol{m}}_i\cdot\hat{\boldsymbol{m}}_{\mathrm{A}_i}\right). \tag{A4}$$

Here, J_{RKKY} is the exchange coupling constant. $\boldsymbol{H}_{\mathrm{RKKY}}$ is considered only in the spin valve shown in Fig. 6(d). $\hat{\boldsymbol{m}}_{\mathrm{A}_i}$ represents the unit magnetization vector of a ferromagnetic layer that is antiferromagnetically coupled with $\boldsymbol{m}_i$, and $J_{\mathrm{RKKY}} = -0.1$ mJ/m^2 is assumed. In the scalar product, the x and y components of $\boldsymbol{r}_i$ in $\hat{\boldsymbol{m}}_i(\boldsymbol{r})$ and $\boldsymbol{r}_{\mathrm{A}_i}$ in $\hat{\boldsymbol{m}}_{\mathrm{A}_i}(\boldsymbol{r}_{\mathrm{A}_i})$ are the same.

[1] Paul A. Merolla *et al.*, A million spiking-neuron integrated circuit with a scalable communication network and interface, Science **345**, 668 (2014).

[2] Frank C. Hoppensteadt and Eugene M. Izhikevich, Oscillatory Neurocomputers with Dynamic Connectivity, Phys. Rev. Lett. **82**, 2983 (1999).

[3] Toru Aonishi, Koji Kurata, and Masato Okada, Statistical Mechanics of an Oscillator Associative Memory with Scattered Natural Frequencies, Phys. Rev. Lett. **82**, 2800 (1999).

[4] Herbert Jaeger and Harald Haas, Harnessing nonlinearity: Predicting chaotic systems and saving energy in wireless communication, Science **304**, 78 (2004).

[5] Wolfgang Maass, Thomas Natschläger, and Henry Markram, Real-time computing without stable states: A new framework for neural computation based on perturbations, Neural. Comput. **14**, 2531 (2002).

[6] Matthew D. Pickett, Gilberto Medeiros-Ribeiro, and R. Stanley Williams, A scalable neuristor built with mott memristors, Nat. Mater. **12**, 114 (2013).

[7] K. Segall, M. LeGro, S. Kaplan, O. Svitelskiy, S. Khadka, P. Crotty, and D. Schult, Synchronization dynamics on the picosecond time scale in coupled Josephson junction neurons, Phys. Rev. E **95**, 032220 (2017).

[8] X. L. Feng, C. J. White, A. Hajimiri, and M. L. Roukes, A self-sustaining ultrahigh-frequency nanoelectromechanical oscillator, Nat. Nanotechnol. **3**, 342 (2008).

[9] J. C. Slonczewski, Current-driven excitation of magnetic multilayers, J. Magn. Magn. Mater. **159**, L1 (1996).

[10] L. Berger, Emission of spin waves by a magnetic multilayer traversed by a current, Phys. Rev. B **54**, 9353 (1996).

[11] S. I. Kiselev, J. C. Sankey, I. N. Krivorotov, N. C. Emley, R. J. Schoelkopf, R. A. Buhrman, and D. C. Ralph, Microwave oscillations of a nanomagnet driven by a spin-polarized current, Nature **425**, 380 (2003).

[12] Jacob Torrejon, Mathieu Riou, Flavio Abreu Araujo, Sumito Tsunegi, Guru Khalsa, Damien Querlioz, Paolo Bortolotti, Vincent Cros, Kay Yakushiji, Akio Fukushima, Hitoshi Kubota, Shinji Yuasa, Mark D. Stiles, and Julie Grollier, Neuromorphic computing with nanoscale spintronic oscillators, Nature **547**, 428 (2017).

[13] Miguel Romera, Philippe Talatchian, Sumito Tsunegi, Flavio Abreu Araujo, Vincent Cros, Paolo Bortolotti, Juan Trastoy, Kay Yakushiji, Akio Fukushima, Hitoshi Kubota, Shinji Yuasa, Maxence Ernoult, Damir Vodenicarevic, Tifenn Hirtzlin, Nicolas Locatelli, Damien Querlioz, and Julie Grollier, Vowel recognition with four coupled spin-torque nano-oscillators, Nature **563**, 230 (2018).

[14] Arkady Pikovsky, *Synchronization A Universal Concept Nonlinear Sciences* (Cambridge University Press, Cambridge, 2003).

[15] Gyorgy Buzsaki, *Rhythms of the Brain* (Oxford University Press, Oxford, 2011).

[16] Gaurav Gupta, Zhifeng Zhu, and Gengchiau Liang, Switching based spin transfer torque oscillator with zero-bias field and large tuning-ratio, arXiv:1611.05169 [cond-mat] (2016).

[17] R. Choi, J. A. Katine, S. Mangin, and E. E. Fullerton, Current-induced pinwheel oscillations in perpendicular magnetic anisotropy spin valve nanopillars, IEEE Trans. Magn. **52**, 1 (2016).

[18] L. Thomas *et al.*, in 2017 IEEE International Magnetics Conference (INTERMAG) (Dublin, 2017).

[19] SPINPM is a micromagnetic code developed by the Istituto P.M. srl (Torino, Italy) based on a fourth-order Runge-Kutta numerical scheme with an adaptative time-step control for the time integration.

[20] J. C. Slonczewski and J. Z. Sun, Theory of voltage-driven current and torque in magnetic tunnel junctions, J. Magn. Magn. Mater. Ser. Proc. 17th Int. Conf. Magn. **310**, 169 (2007).

[21] Robert M. May, Simple mathematical models with very complicated dynamics, Nature **261**, 459 (1976).

[22] W. R. Softky and C. Koch, The highly irregular firing of cortical cells is inconsistent with temporal integration of random EPSPs, J. Neurosci. **13**, 334 (1993).

[23] John M. Beggs, The criticality hypothesis: How local cortical networks might optimize information processing, Philos. Trans. R. Soc. A: Math. Phys. Eng. Sci. **366**, 329 (2008).

[24] Chris G. Langton, Computation at the edge of chaos: Phase transitions and emergent computation, Phys. D: Nonlinear Phenom. **42**, 12 (1990).

[25] Nils Bertschinger and Thomas Natschläger, Real-time computation at the edge of chaos in recurrent neural networks, Neural Comput. **16**, 1413 (2004).

[26] Suhas Kumar, John Paul Strachan, and R. Stanley Williams, Chaotic dynamics in nanoscale NbO_2 mott memristors for analogue computing, Nature **548**, 318 (2017).

[27] J. J. Collins, Carson C. Chow, and Thomas T. Imhoff, Stochastic resonance without tuning, Nature **376**, 236 (1995).
[28] Feng Liu, Bambi Hu, and Wei Wang, Effects of correlated and independent noise on signal processing in neuronal systems, Phys. Rev. E **63**, 031907 (2001).
[29] Kazuyoshi Ishimura, Alexandre Schmid, Tetsuya Asai, and Masato Motomura, Stochastic resonance induced by internal noise in a unidirectional network of excitable FitzHugh-nagumo neurons, NOLTA **7**, 164 (2016).
[30] K. Ishimura, Dr. Thesis, Graduate School of Information Science and Technology, Hokkaido University, Hokkaido, 2016 [in Japanese].
[31] Richard B. Stein, E. Roderich Gossen, and Kelvin E. Jones, Neuronal variability: Noise or part of the signal? Nat. Rev. Neurosci. **6**, 389 (2005).
[32] L. Appeltant, M. C. Soriano, G. Van der Sande, J. Danckaert, S. Massar, J. Dambre, B. Schrauwen, C. R. Mirasso, and I. Fischer, Information processing using a single dynamical node as complex system, Nat. Commun. **2**, 468 (2011).
[33] M. N. Baibich, J. M. Broto, A. Fert, F. Nguyen Van Dau, F. Petroff, P. Etienne, G. Creuzet, A. Friederich, and J. Chazelas, Giant Magnetoresistance of (001)Fe/(001)Cr Magnetic Superlattices, Phys. Rev. Lett. **61**, 2472 (1988).
[34] G. Binasch, P. Grünberg, F. Saurenbach, and W. Zinn, Enhanced magnetoresistance in layered magnetic structures with antiferromagnetic interlayer exchange, Phys. Rev. B **39**, 4828 (1989).
[35] T. Miyazaki and N. Tezuka, Giant magnetic tunneling effect in $Fe/Al_2O_3/Fe$ junction, J. Magn. Magn. Mater. **139**, L231 (1995).
[36] J. S. Moodera, Lisa R. Kinder, Terrilyn M. Wong, and R Meservey, Large Magnetoresistance at Room Temperature in Ferromagnetic Thin Film Tunnel Junctions, Phys. Rev. Lett. **74**, 3273 (1995).
[37] Shinji Yuasa, Taro Nagahama, Akio Fukushima, Yoshishige Suzuki, and Koji Ando, Giant room-temperature magnetoresistance in single-crystal Fe/MgO/Fe magnetic tunnel junctions, Nat. Mater. **3**, 868 (2004).
[38] Stuart S. P. Parkin, Christian Kaiser, Alex Panchula, Philip M. Rice, Brian Hughes, Mahesh Samant, and See-Hun Yang, Giant tunnelling magnetoresistance at room temperature with MgO (100) tunnel barriers, Nat. Mater. **3**, 862 (2004).
[39] David D. Djayaprawira, Koji Tsunekawa, Motonobu Nagai, Hiroki Maehara, Shinji Yamagata, Naoki Watanabe, Shinji Yuasa, Yoshishige Suzuki, and Koji Ando, 230%room-temperature magnetoresistance in CoFeB/MgO/CoFeB magnetic tunnel junctions, Appl. Phys. Lett. **86**, 092502 (2005).
[40] E. B. Myers, D. C. Ralph, J. A. Katine, R. N. Louie, and R. A. Buhrman, Current-induced switching of domains in magnetic multilayer devices, Science **285**, 867 (1999).
[41] S. Mangin, D. Ravelosona, J. A. Katine, M. J. Carey, B. D. Terris, and Eric E. Fullerton, Current-induced magnetization reversal in nanopillars with perpendicular anisotropy, Nat. Mater **5**, 210 (2006).
[42] Mark D. Stiles and Jacques Miltat, in *Spin Dynamics in Confined Magnetic Structures III*, Topics in Applied Physics, Vol. 101, edited by Burkard Hillebrands and André Thiaville (Springer, Berlin, Heidelberg, 2006), p. 225.
[43] M. Beleggia, M. De Graef, Y. T. Millev, D. A. Goode, and G. Rowlands, Demagnetization factors for elliptic cylinders, J. Phys. D: Appl. Phys. **38**, 3333 (2005).
[44] J. Z. Sun, Spin-current interaction with a monodomain magnetic body: A model study, Phys. Rev. B **62**, 570 (2000).
[45] M. Ignatov, M. Hansen, M. Ziegler, and H. Kohlstedt, Synchronization of two memristively coupled van der pol oscillators, Appl. Phys. Lett. **108**, 084105 (2016).
[46] Marina Ignatov, Martin Ziegler, Mirko Hansen, and Hermann Kohlstedt, Memristive stochastic plasticity enables mimicking of neural synchrony: Memristive circuit emulates an optical illusion, Sci. Adv. **3**, e1700849 (2017).
[47] Eric Arturo Montoya, Salvatore Perna, Yu-Jin Chen, Jordan A. Katine, Massimiliano d'Aquino, Claudio Serpico, and Ilya N. Krivorotov, Magnetization reversal driven by low dimensional chaos in a nanoscale ferromagnet, arXiv:1806.03383 [cond-mat] (2018).
[48] Rie Matsumoto, Hiroko Arai, Shinji Yuasa, and Hiroshi Imamura, Efficiency of Spin-Transfer-Torque Switching and Thermal-Stability Factor in a Spin-Valve Nanopillar with First- and Second-Order Uniaxial Magnetic Anisotropies, Phys. Rev. Appl. **7**, 044005 (2017).
[49] J.-P. Eckmann, S. Oliffson Kamphorst, and D. Ruelle, Recurrence plots of dynamical systems, Europhys. Lett. **4**, 973 (1987).
[50] Norbert Marwan, M. Carmen Romano, Marco Thiel, and Jürgen Kurths, Recurrence plots for the analysis of complex systems, Phys. Rep. **438**, 237 (2007).
[51] C. L. Webber and J. P. Zbilut, Dynamical assessment of physiological systems and states using recurrence plot strategies, J. Appl. Physiol. **76**, 965 (1994).
[52] Norbert Marwan and Jürgen Kurths, Nonlinear analysis of bivariate data with cross recurrence plots, Phys. Lett. A 302, 299 (2002).
[53] Alan Wolf, Jack B. Swift, Harry L. Swinney, and John A. Vastano, Determining lyapunov exponents from a time series, Phys. D: Nonlinear Phenom. **16**, 285 (1985).
[54] E. M. Izhikevich, Which model to use for cortical spiking neurons? IEEE Trans. Neural Networks **15**, 1063 (2004).
[55] N. Locatelli, V. Cros, and J. Grollier, Spin-torque building blocks, Nat. Mater. **13**, 11 (2014).
[56] J. Grollier, D. Querlioz, and M. D. Stiles, Spintronic nanodevices for bioinspired computing, Proc. IEEE **104**, 2024 (2016).